

A Methodology for the Design of a Single-Sided Axial-Flux Permanent Magnet (AFPM) Motor for Lathe Machines

1st Ali Jamali-Fard

*Electrical Machines and Transformer-
Research Laboratory (EMTRL)
Department of Electrical Engineering,-
Amirkabir University of Technology
Tehran, Iran
a.jamalifard@aut.ac.ir*

2nd Mojtaba Mirsalim

*Electrical Machines and Transformer-
Research Laboratory (EMTRL)
Department of Electrical Engineering,-
Amirkabir University of Technology
Tehran, Iran
mirsalim@aut.ac.ir*

Abstract—A single-sided axial-flux permanent magnet (AFPM) motor with a fractional slot concentrated winding (FSCW) is a suitable choice for low-speed and high-torque applications such as lathe machines. Having a disc-type structure with an FSCW allows increasing the number of poles to reduce the motor volume. There are various equivalent two-dimensional (2-D) models for the analysis of single-sided AFPM motors, but because of the complex structure, the optimal design of this motor type requires several three-dimensional (3-D) analyses. For example, using 2-D FEA for estimating magnets' eddy current losses and consequently, the motor efficiency could be misleading in the design process. This paper aims to provide a design workflow based on a combination of 2-D and 3-D FEA for the optimal design of a single-sided AFPM motor. The purpose is to segregate the calculation of different motor parameters such as magnetic loading, d- and q-inductance, static torque curve, efficiency, etc. from each other. This segregation makes the right selection of the proper model for the calculation of each motor parameter possible, which leads to a well-targeted design workflow. To evaluate the performance of the proposed method, a 4kW-750rpm motor for the lathe machine is designed. Simulation results are presented and discussed.

Index Terms—Axial-flux, permanent magnet motor, finite element analysis (FEA), lathe machine.

NOMENCLATURE

P_{out} [kW] — Rated output power
 rpm [rpm] — Base speed
 T_{out} [Nm] — Rated output torque
 V_{dc} [V] — DC link voltage
 η_d [—] — Desired efficiency
 $\cos(\phi)$ [—] — Desired power factor
 B_{av} [T] — Magnetic loading
 ac [kA/m] — Electric loading
 J_{sw} [A/mm²] — Stator winding current density
 N_s [—] — Number of stator slots
 p [—] — Number of rotor poles
 ISD [mm] — Inner stator diameter
 OSD [mm] — Outer stator diameter

$sr = ISD/OSD$ — Split ratio
 IRD [mm] — Inner rotor diameter
 ORD [mm] — Outer rotor diameter
 d_m [mm] — Depth of magnets
 d_{ry} [mm] — Depth of rotor yoke
 d_{sy} [mm] — Depth of stator yoke
 d_{ss} [mm] — Depth of stator slot
 w_{ss} [mm] — Width of stator slot
 d_c [mm] — Depth of coil
 w_c [mm] — Width of coil
 E_{ph} [V] — Phase back-EMF
 V_{ph} [V] — Phase voltage
 $\gamma_{emf} = E_{ph}/V_{ph}$ — Back-EMF ratio
 R_{ph} [Ω] — Phase resistance
 L_d [H] — Direct axis inductance
 L_q [H] — Quadrature axis inductance
 Λ_M [Wb] — Flux linkage due to magnets
 k_w [—] — Winding factor
 N_{tc} [—] — Number of turns per coil
 N_{tph} [—] — Number of effective turns per phase
 $N_{strands}$ [—] — Number of parallel strands
 N_p [—] — Number of parallel branches
 K_{fill} [—] — Winding fill factor
 d_w [mm] — Wire diameter

I. INTRODUCTION

Axial-flux permanent magnet (AFPM) motors are well-suited for various applications such as traction, hybrid electric vehicles, appliances, and defense [1]–[5] because of several advantages: (i) compact structure [6], [7], (ii) high torque and high power density, (iii) low maintenance, and (iv) high efficiency [8]–[10]. The role of AFPM motors is especially prominent in applications where the integration of motors with other mechanical parts is imperative [11]. The objective of this research is the lathe machine, with the goal to design an AFPM motor for driving the chuck. An attractive feature of AFPM motors is the possibility of using non-overlapping

* Corresponding Author: Ali Jamali-Fard

fractional slot concentrated winding (FSCW). An FSCW has the minimum end-winding length, resulting in reduced copper losses and reaching higher efficiency classes [12]. The non-overlapping aspect of an FSCW makes the motor more tolerant against phase-to-phase short circuit faults, enhancing its reliability.

There are several methods presented in the literature for modeling, analysis, sizing, and optimal design of AFPM motors [3], [7], [11], [13]–[16]. In [16] a design optimization approach using a differential evolution algorithm is implemented. A simple procedure for nonlinear magnetic analysis of axial-flux permanent-magnet machines as an assistant design tool of 3-D finite-element analysis (3D-FEA) is introduced in [15]. The proposed algorithm is based on the magnetic equivalent circuit (MEC) and an analytical model of air-gap permeances, including saturable permeances in the core. It is shown that the computation time for the calculation of motor characteristics is reduced significantly. Although, the MEC method is fast, it highly depends on geometry and especially the slot shapes, and it cannot be considered a general-purpose method like FEA. Quantities such as torque ripple cannot be calculated by the MEC method with good accuracy. The authors of [11] proposed a 2-D analytical model based on the solution of Maxwell’s equations using magnetic vector potential and closed-form solution. The model is derived using the Fourier Transform to determine the torque and other electrical and mechanical parameters produced by the AFPM motor.

In most of the aforementioned methods, the goal is to develop either a 2-D or 3-D analytic model using techniques like MEC or Fourier series analysis. However, while these methods are fast, they exhibit limited accuracy in calculating certain critical and deterministic parameters of the motor during the design process, such as torque ripple or eddy current losses in the magnets. In these methods, many assumptions must be made to simplify the problem. Furthermore, when the designer changes the motor’s topology, reformulations are necessary to adapt the model to the new structure.

This paper aims to provide a design workflow based on a combination of 2-D and 3-D finite element calculations for the optimal design of a single-sided AFPM motor with an FSCW. FEA is a general-purpose method capable of adapting to complex geometries. Therefore, modeling time is not a concern compared to other methods, such as MEC [17]. In this work, the purpose is to segregate the calculation of motor characteristics from each other to select the right model for calculating each of them. For example, the magnetic loading of the motor could be calculated by running a magneto-static analysis of the 2-D model. However, for the calculation of eddy current losses in magnets, we have to run a transient time-stepping simulation on a 3-D model [18]–[21]. Combining different models for the derivation of motor performance curves and parameters can lead us to a well-targeted design workflow which is presented in this paper. To investigate the fulfillment of the proposed method, a case-study motor applicable to lathe machine application is selected, designed, and optimized. The simulation results of the design process

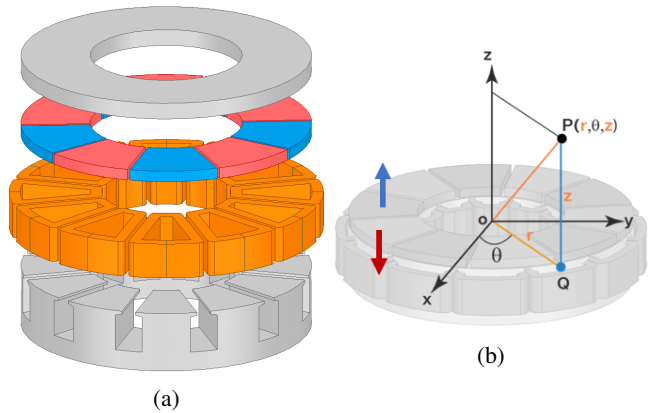


Fig. 1: The motor structure; (a) exploded view of the active parts, (b) the magnetization direction

TABLE I: Properties of the case-study motor

Parameter	Value	Parameter	Value
P_{out}	4kW	rpm	750rpm
T_{out}	51Nm	V_{dc}	324V
η_d	90%	Stator material	M530-50A
Rotor material	steel 1010	Magnet grade	N38
N_s	12	p	10

and optimal sample are presented and discussed in detail.

II. MOTOR STRUCTURE

Fig. 1a illustrates the exploded view of the active parts of a single-sided AFPM motor. The stator core is slotted, and it includes a double-layer three-phase winding. The number of winding coils is equal to the number of stator teeth. The stator/rotor cores of AFPM motors can be made of different magnetic materials, such as laminated electrical steel (ES), soft magnetic composite (SMC) powders, and solid iron [22]. In this work, it is assumed the stator core is made of laminated electrical steel, and the rotor core is simply a solid iron with magnets glued on it. The magnets are magnetized in axial direction as shown in Fig. 1b.

To investigate the performance of the proposed technique, a 4kW-750rpm motor is considered as a case-study. The application of this motor is driving the chuck of the lathe machine. The parameters of this motor are presented in Table I. As seen, the rated output torque of the motor at the base speed is 51Nm. The motor is required to deliver this torque from zero to the base speed. The voltage of the DC link is 324V, and the RMS value of the phase voltage is 220V. The desired efficiency of the motor at rated conditions should be above 90%. Desired power factor could be considered equal to one.

III. PROPOSED METHOD

The main aim of this work is to construct a well-targeted workflow for the electromagnetic design of single-sided AFPM motors by combining 2-D and 3-D finite element calculations.

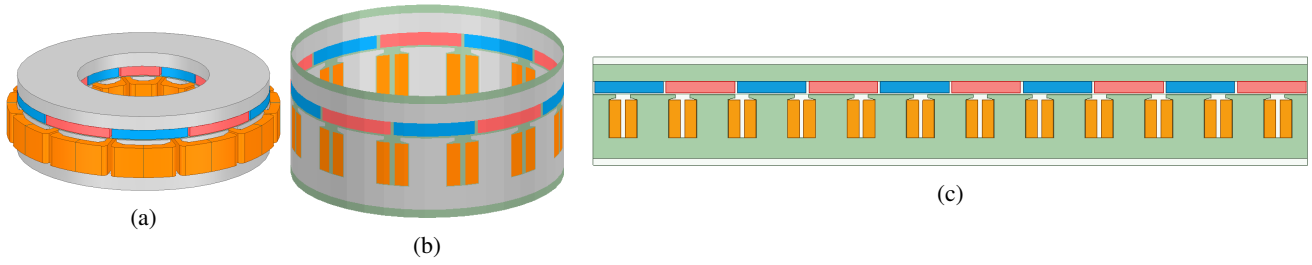


Fig. 2: 2-D and 3-D models of the case-study motor: (a) 3-D full model, (b) circumferential cross-section surface, (c) 2-D linear model

The first step in this method is the generation of 2-D and 3-D finite element models of the motor. Fig. 2a shows the 3-D full model, Fig. 2b illustrates a circumferential cross-section necessary for the creation of the 2-D model, and Fig. 2c represents the linear 2-D model.

The flowchart of the entire design process is shown in Fig. 3. It comprises 26 steps, and the design workflow involves four types of finite element analyses, including 2-D and 3-D magneto-static and transient simulations. The steps of this flowchart is as follows:

- 1) In this step, we set the electrical and mechanical constraints. For example, one electrical constraint is the voltage of the DC link, and one mechanical constraint is the inner diameter of the stator core. Since our objective is to directly connect the motor to the chuck of the lathe machine, the inner diameter of the hollow area inside the motor must be larger than the diameter of the center hole of the chuck. In the case-study motor, the diameter of the center hole of the chuck is 80mm.
- 2) Design targets are the nameplate parameters that must be satisfied. These parameters include P_{out} , T_{out} , rpm , η_d , etc.
- 3) In this step, we set or modify the values of decision variables such as B_{av} , ac , K_{fill} , J_{sw} , etc. Initially, setting is performed for the first iteration of the design. During this initial iteration, appropriate initial values must be selected to yield a well-performing seed motor for further optimization. In subsequent iterations, adjustments are made based on feedback obtained from the following steps to ensure that the decision conditions are satisfied.
- 4) The sizing of the motor using analytic equations is performed in this step. A detailed explanation is presented in Appendix B.
- 5) The first FEA involves calculating the magnetic loading using the 2-D magneto-static solver, which is done in this step. In this simulation type, we can employ a very fine mesh in the air gap and calculate the waveform of the z-component of the flux density in the air gap due to magnets. Because we are running a 2-D FEA model, the simulation is fast.
- 6) The value of magnetic loading calculated by the 2-D FEA model need not necessarily be equal to our assumption. This is because the 2-D model is a sim-

plified representation, neglecting the existence of the radial component of flux density. In this step, we check whether the calculated value of B_{av} is within a 20% error of our assumption. If yes, we continue with the design; otherwise, we should modify our assumptions to ensure that the calculated value falls within an acceptable range.

- 7) In this step, we conduct a 3-D magneto-static simulation to calculate the magnetic loading. In the 3-D model, all components of flux density are calculated. The purpose of using the 2-D model for the magnetic loading calculation in step 5 is to reduce the number of runs of the 3-D model in this step. While the 2-D model has some limitations, it provides a faster guide to achieving the desired design.
- 8) Unlike step 6, the value of magnetic loading calculated by the 3-D model should be equal to the assumed value. If the value is equal, we proceed to the next iteration; otherwise, if there is a significant deviation, we should modify our assumption and perform the analytic design again.
- 9) During the sizing of the motor, we assume maximum permissible flux density levels at different locations of the rotor and stator cores. The permissible values are close to the knee point of the B-H curves of the magnet materials. If the flux density levels are below and close to the permissible values, we proceed to the next step; otherwise, if we have significant saturation or even if we have low flux density levels, we should modify our assumptions and redo the design. Deep saturations result in high magneto-motive force (MMF) drops, and low flux density levels indicate overdesign.
- 10) When the flux density levels in the stator teeth, stator back iron, or rotor core exceed the permitted values, we should increase the size of the iron cores to reduce the MMF drops in these parts and keep the flux density levels below the permitted values. Similarly, if the flux density levels are considerably lower than the permissible values, we should reduce the size of iron parts to avoid overdesign.
- 11) In this step, we calculate the static torque curve by performing 2-D magneto-static simulations. We set the value of the current amplitude equal to the rated value and change the current angle from zero to 180 electric

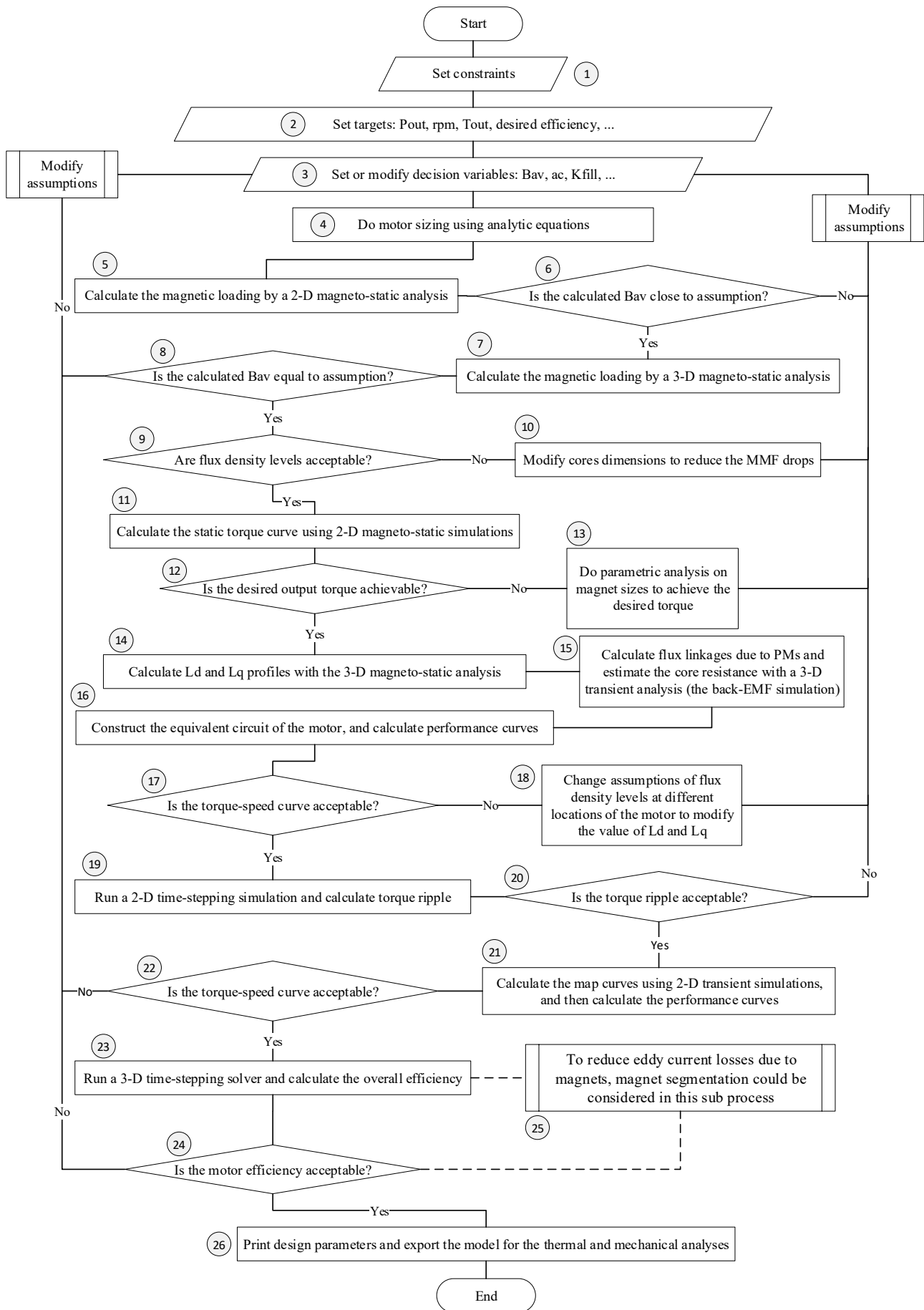


Fig. 3: The flowchart of the proposed method for design of an AFPM Motor with an FSCW

degrees.

- 12) After calculating the static torque curve, we can compare the maximum value of the electric torque that the motor can generate at the rated current (which occurs when the current angle is equal to 90) with the desired value of electric torque mentioned in the design targets. If the desired torque is achievable, we can continue with the design; otherwise, we should modify our assumptions and redo the design process.
- 13) The total energy density available in the air gap is proportional to the volume of magnets. When, for a specific value of electric loading, the desired torque is not achievable, we should conduct a parametric analysis on magnet dimensions to find the correct values, especially focusing on the magnets' depth. This parametric analysis can be performed using 2-D magneto-static simulations. In these simulations, we set the value of the stator current angle equal to 90 electric degrees.
- 14) In this step, we calculate the profiles of L_d and L_q as functions of the stator current phasor amplitude using 3-D magneto-static simulations.
- 15) The flux linkage curves, and induced voltage waveforms due to magnets only are calculated in this step by a transient no-load simulation using the 3-D model.
- 16) In this step, we calculate the performance curves of the motor, such as the torque-speed curve, by solving the equivalent circuit model (Appendix C) of the motor. The values of parameters in the equivalent circuit are calculated in two previous steps. Solving the equivalent circuit is efficient, allowing us to quickly evaluate the performance of the motor at different speeds.
- 17) In this step, we analyze the torque-speed curve of the motor. From zero to the base speed, we should have the rated torque (constant torque region), and at the base speed, the motor should deliver the rated power for the rated current. If operation in the field weakening region is of interest, the maximum achievable speed and the efficiency map should be analyzed as well.
- 18) When the torque-speed curve is not acceptable, there are several probable reasons. For instance, when the number of turns per coil is high, the value of phase back-EMFs is also high, and the supply may not be able to inject rated currents into the winding at the base speed. From the equivalent circuit point of view, we should modify circuit parameters to achieve the desired torque-speed curve. For example, we compare the values of L_d and L_q with the desired values that we need, and based on this comparison, we modify the assumptions.
- 19) Calculating torque ripple with sufficient accuracy requires a fine mesh in the air gap and a small time step size. However, employing a fine mesh in a 3-D transient FEA model with a small time step size increases the simulation time. Therefore, in this step, a proper choice is to use the 2-D transient FEA model to evaluate the value of torque ripple.
- 20) In this step, we compare the calculated value of torque ripple with the maximum permissible value. If the torque ripple is lower than the permissible value, we continue with the design; otherwise, we should modify our assumptions to reduce the torque ripple. For example, one approach could be modifying the shape of the stator tooth shoe.
- 21) In step 16, we calculated the performance curves of the motor, such as the torque-speed curve, using the equivalent circuit model. We derived L_d and L_q profiles as functions of phase current amplitude. However, it's important to note that this model does not consider the effect of cross-magnetization. Additionally, the effect of torque ripple is neglected in the torque map. The aim of this step is to recalculate the performance curves using the 2-D transient FEA model with greater accuracy.
- 22) This step is similar to step 17. The difference lies in the fact that the torque-speed curve analyzed in this step has higher accuracy, and the sample design reached at this step has an acceptable value of torque ripple.
- 23) In this step, we calculate the overall efficiency of the motor by performing a 3-D time-stepping transient simulation. In all of the previous steps, we didn't concern ourselves with the motor efficiency because accurate estimations of the motor efficiency rely on the exact calculation of eddy current losses in magnets. In this simulation, we should consider a fine mesh and a fine time step size as well.
- 24) In this step, we compare the calculated overall efficiency with the acceptable value. If the efficiency is within an acceptable range, we proceed with the design; otherwise, we should run a sub procedure to increase the motor efficiency or reconsider our assumptions and restart the design flowchart from the beginning.
- 25) When the efficiency is lower than the acceptable value, the relative amplitudes of different loss types should be compared. Appropriate modifications should be considered to reduce losses. For example, if the copper losses in the stator winding are considerable, we should reduce the assumed value of current density in the initial stage of the design. Similarly, when the value of eddy current losses in magnets is high, methods such as magnet segmentation can be employed.
- 26) When everything is in order, in this step, we print design parameters and export the model for the next analysis types, such as mechanical and thermal.

IV. RESULTS AND DISCUSSION

In this section, simulation results are presented and discussed. Fig. 4a shows the flux density and flux lines due to magnets derived by the 2-D magneto-static analysis. In this simulation, the stator current is zero and the aim is to calculate the waveform of the axial component of flux density in the air gap. As is seen in Fig. 4a, flux density levels in iron parts are below the permissible values. Fig. 4b represents the waveform of flux density in the air gap.

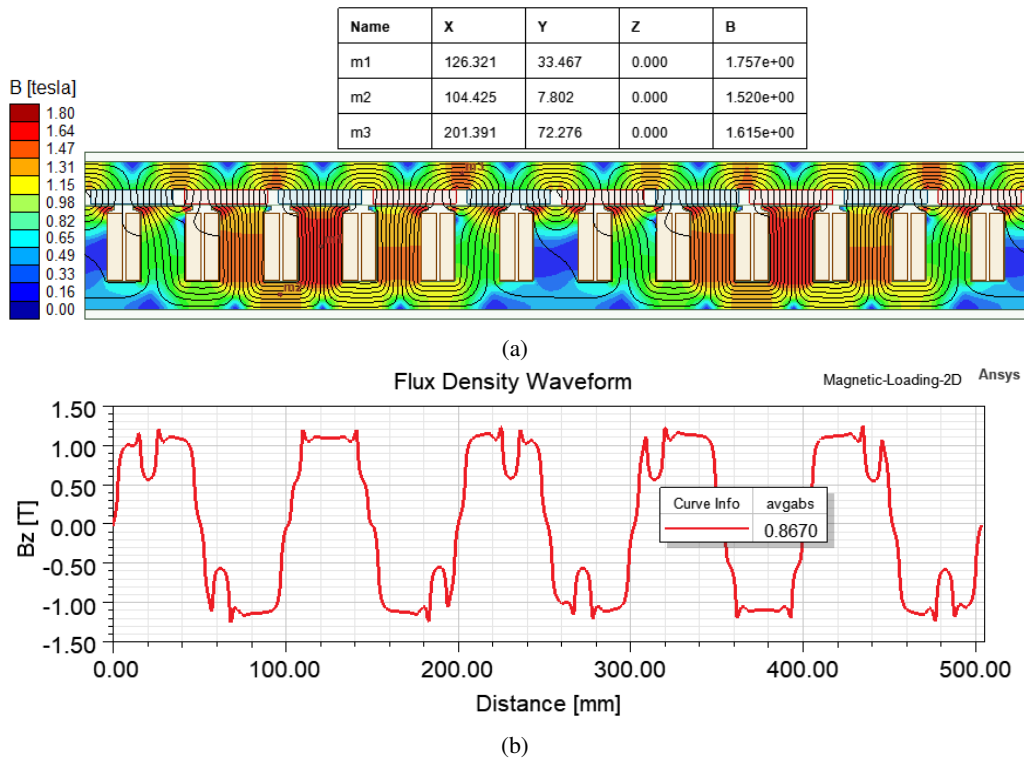


Fig. 4: No-load magneto-static analysis of 2-D model: (a) flux lines and flux density magnitude, (b) flux density waveform in air gap

Fig. 5 shows the streamlines of the flux density field, in the middle of the structure. Fig. 6 illustrates the magnitude of flux density on a surface in the middle of the air gap. The aim of this simulation is to calculate the magnetic loading with a more accuracy compared to 2-D analysis.

The next step in the design workflow involves visualizing the amplitude of the flux density in the iron parts of the motor to check the level of saturation. To do this, we should first consider candidate paths. Circular candidate paths are considered in the back irons of the rotor and stator cores, while line paths are considered in the middle of stator teeth. Fig. 7 shows all candidate paths and amplitude of the flux density on them. As observed, the maximum values are within the permissible range, and we can proceed with the design.

Fig. 8a shows the calculated static torque curve using the 2-D model. As is seen, the maximum torque for the rated current is close to the desired rated torque. When the motor cannot generate the desired torque, a quick parametric analysis that can be done at this step is sweeping over the magnet depth to find a proper size for it. Fig. 8b shows an example of a parametric study by changing the d_m . As observed, the desired torque is achievable when the magnet depth is between 7 to 8mm.

Fig. 9 represents the flux linkage curves calculated in no-load simulation. The maximum value of these waveforms is the Λ_M in the equivalent circuit. To complete the equivalent circuit, we need to calculate L_d and L_q profiles. Fig. 10a and Fig. 10b show the L_d and L_q profiles as a function of current

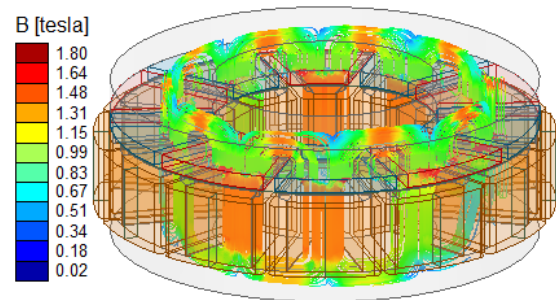


Fig. 5: Streamlines of flux density field

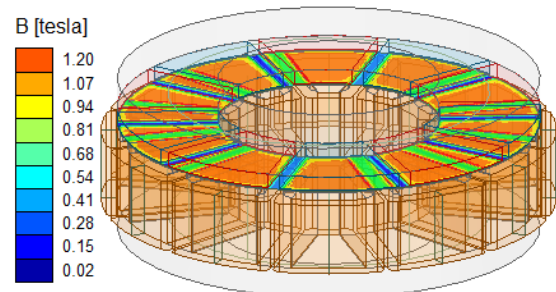


Fig. 6: Magnitude of the flux density in the air gap

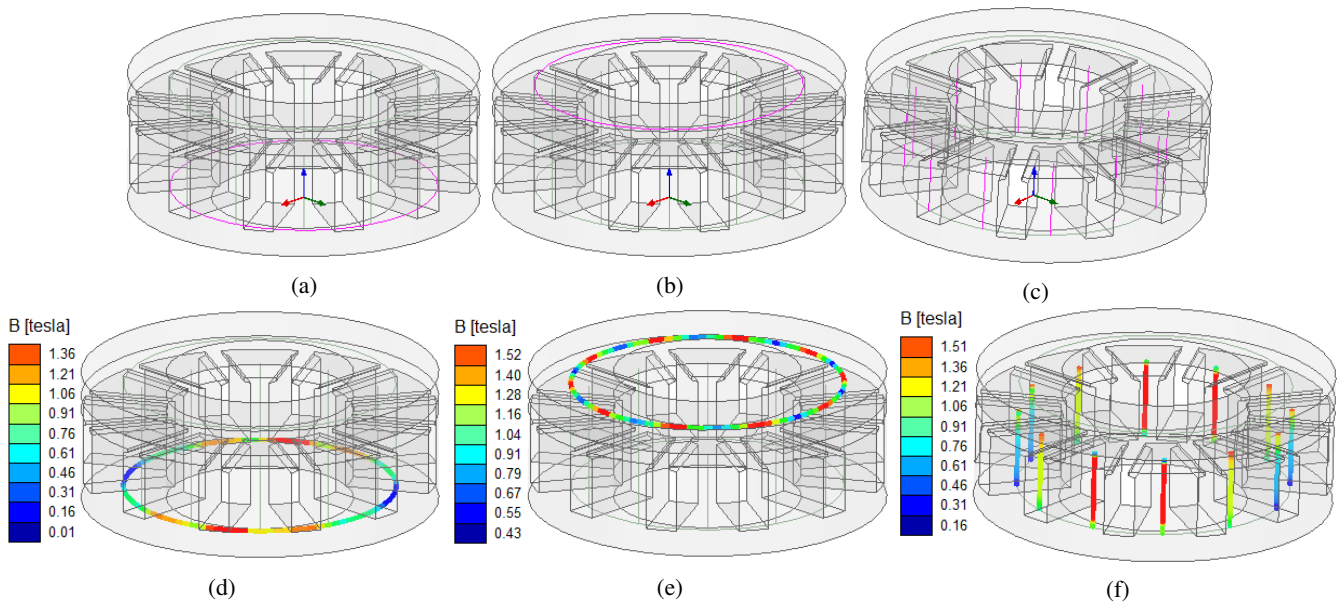


Fig. 7: (a), (b), and (c) are candidate paths to visualize the level of saturation in iron parts; (d), (e), and (f) magnitude of flux density on candidate paths

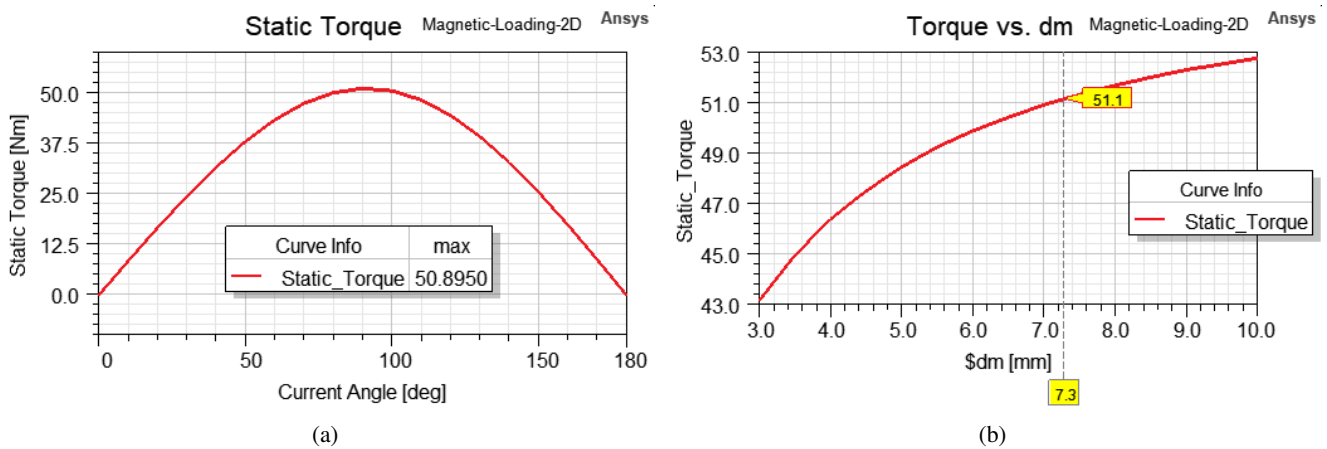


Fig. 8: Magnet sizing process: (a) the static torque curve, (b) Maximum developed torque versus d_m

level calculated by the 3-D magneto-static solver, respectively. When the equivalent circuit is ready, we can solve it for different speeds to calculate the torque-speed and power-speed curves. Fig. 11a represents the calculated torque-speed curve for different current levels. As seen, the motor can deliver the rated torque at the base speed.

When the torque-speed curve is acceptable, the next analysis type is the calculation of torque ripple. Fig. 12 shows the electric torque profile calculated by a 2-D steady-state simulation. In this simulation, a fine mesh in the air gap and a fine time step size for the solver are considered to calculate the torque profile with enough accuracy. As is seen, while the average torque is 51Nm, the peak-to-peak value of torque ripple is below 2.4Nm, in other words, the torque ripple is below 5%.

When the torque ripple is acceptable, the next step is recalculation of the torque-speed curve using the FEA model

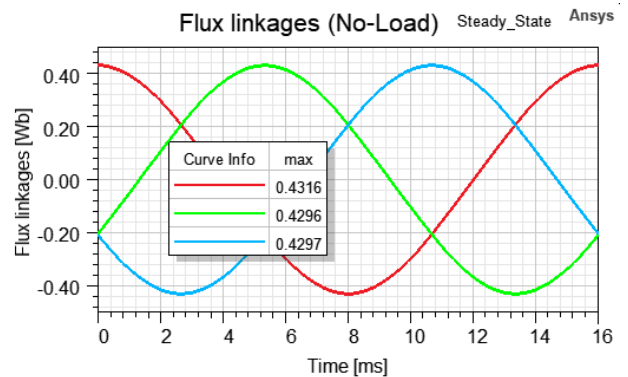


Fig. 9: Flux linkage waveforms derived by no-load simulation

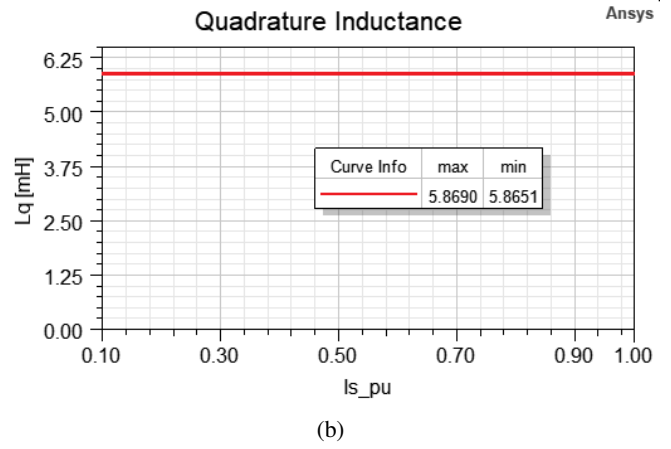
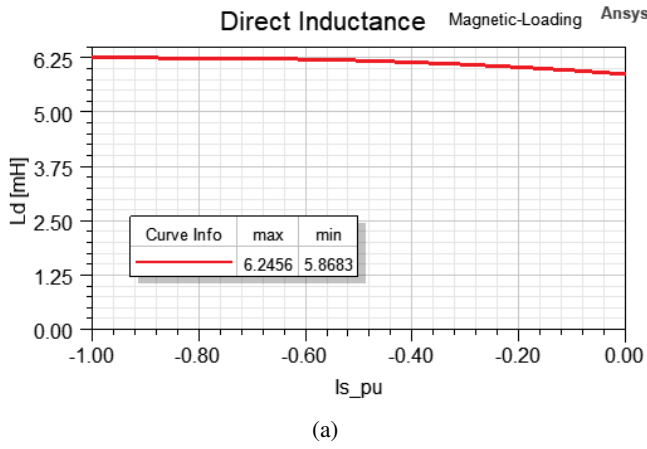


Fig. 10: Inductance profiles versus current level: (a) L_d profile, (b) L_q profile

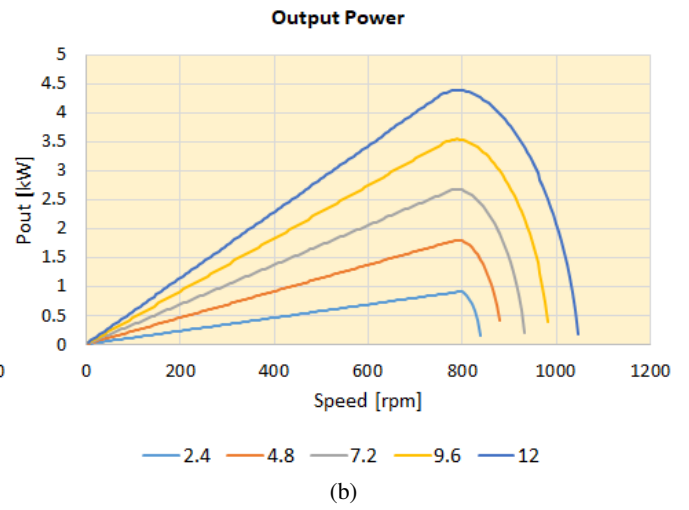
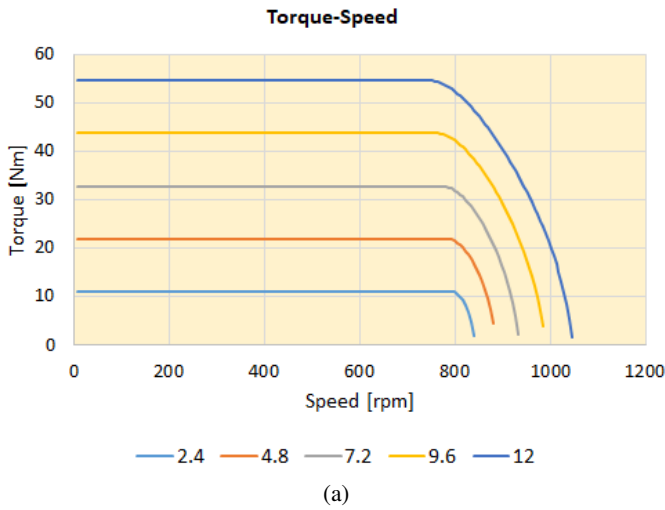


Fig. 11: Performance curves derived by solving the equivalent circuit for different speeds, considering different current levels: (a) torque-speed curve, (b) power-speed curve

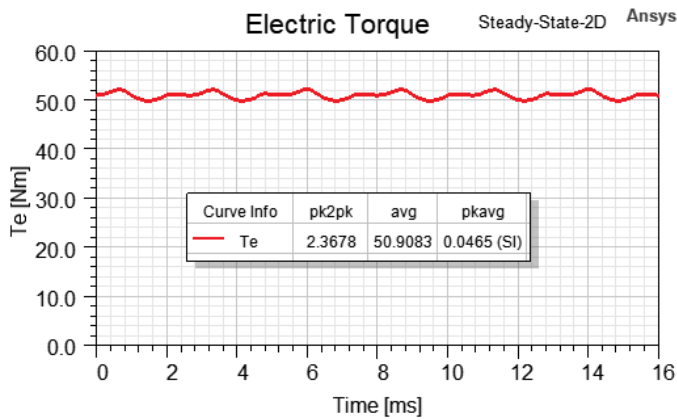


Fig. 12: Electric torque profile calculated by a 2-D steady-state simulation

instead of using the equivalent circuit model to include the effect of cross-magnetization. Fig. 13a illustrates the torque map, and Figs. 13b and 13c show the flux linkage maps calculated by performing 2-D time-stepping FEA simulations. In these simulations, we change the values of direct and quadrature currents in the second quadrant. Then, by conducting the simulations and calculating average values, we can generate contour plots, and finally construct the following functions:

$$T_e(i_d, i_q), \quad \lambda_d(i_d, i_q), \quad \lambda_q(i_d, i_q) \quad (1)$$

Where, T_e is the developed electric torque, λ_d is the d-axis flux linkage, λ_q is the q-axis flux linkage, and i_d and i_q are d and q components of the phase current. Using (1), we can include the effect of cross-magnetization and calculate the new performance curves. Fig. 14a shows the new torque-speed curve calculated using the map curves. As is seen, the motor is able to deliver the rated torque from the zero to the base speed.

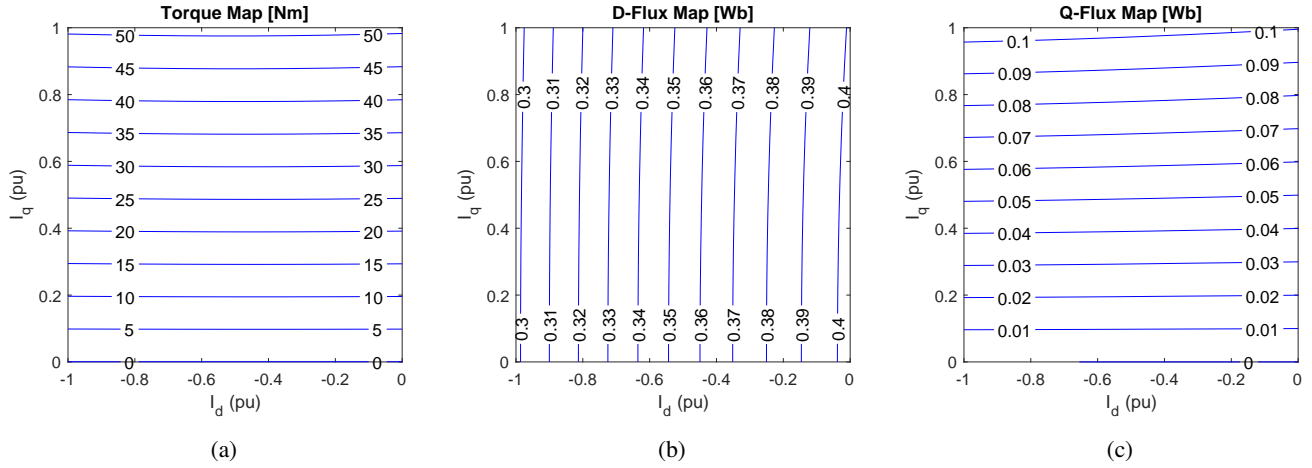


Fig. 13: Map curves calculated by performing 2-D steady-state simulations: (a) torque map, (b) d-axis flux linkage map, (c) q-axis flux linkage map

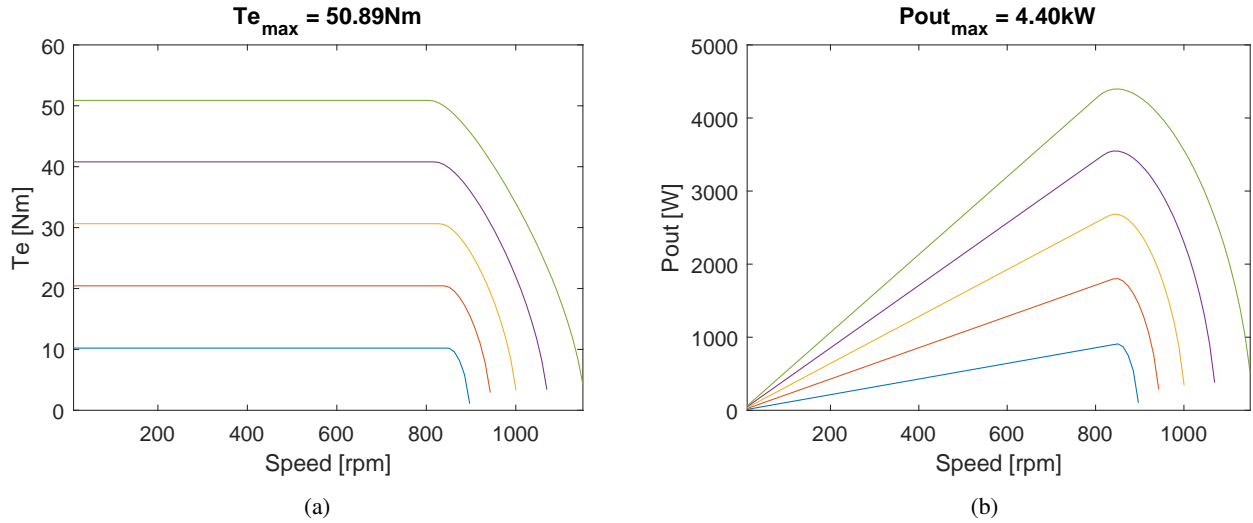


Fig. 14: Performance curves calculated by map curves: (a) torque-speed curve, (b) power-speed curve

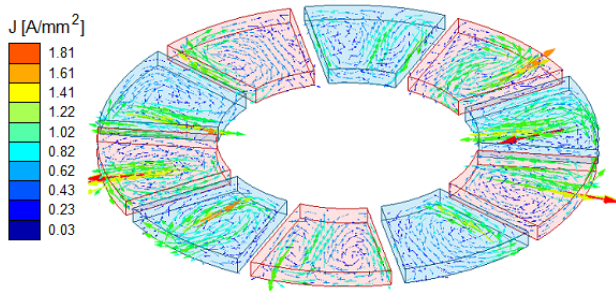


Fig. 15: Induced eddy currents in magnets

To complete the design process, in the final stage, we run a 3-D transient simulation considering iron loss and eddy current loss calculations to evaluate the motor efficiency. Fig. 15 represents the induced eddy current in one magnet in this simulation. The calculated efficiency is equal to 92.7%. The

TABLE II: Parameters of the designed case-study motor

Parameter	Value	Parameter	Value
ISD	110mm	OSD	210mm
w_{ss}	18mm	d_{ss}	40mm
d_{sy}	14mm	d_{ry}	14mm
d_m	7mm	g	1.2mm
N_{IC}	58	$N_{strands}$	4
N_p	1	d_w	0.81mm

parameters of the designed case-study motor are given in Table II.

V. CONCLUSION

In this paper, a workflow for the design of axial-flux permanent magnet (AFPM) motors with a fractional slot

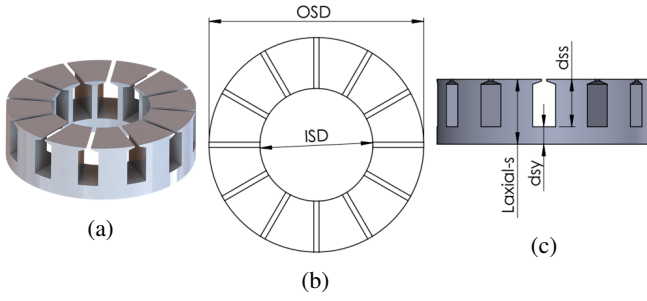


Fig. 16: Geometrical dimensions of the stator core: (a) isometric view, (b) top view, (c) side view

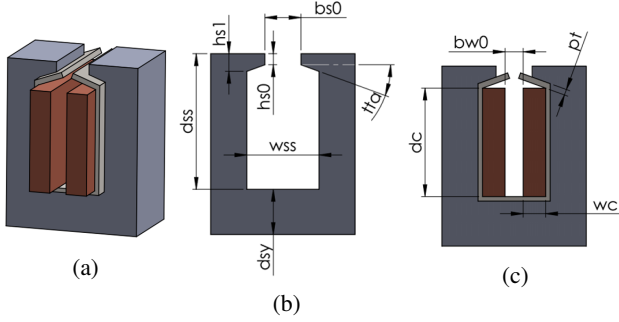


Fig. 17: Geometrical dimensions of the stator winding: (a) isometric view, (b) slot dimensions, (c) coil dimensions

concentrated winding (FSCW) was presented. The aims were to develop a well-targeted method based on 2-D and 3-D finite element calculations, and calculating different parameters of the motor with the right model. A 4kW-750rpm case-study motor was designed for the lathe machine using the proposed method. As shown, the method can generate an appropriate seed design after a few iterations. One of the advantages of the proposed method is to avoid running 3-D time-stepping finite element simulations by implementing the corresponding simplified simulations (either 2-D or 3-D magneto-statics).

APPENDIX A GEOMETRICAL DIMENSIONS

Geometrical parameters of the stator core, stator winding, and rotor core are shown in Fig. 16, 17, and 18, respectively.

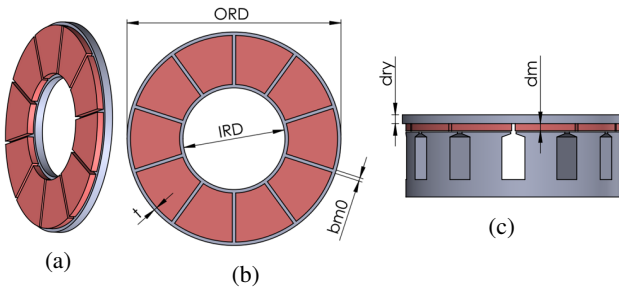


Fig. 18: Geometrical dimensions of the rotor core: (a) isometric view, (b) top view, (c) side view

APPENDIX B ANALYTIC SIZING

The procedure for sizing of the motor is as follows:

- 1) Calculation of the rated output torque:

$$T_{out} = P_{out}/\omega_m \quad (2)$$

here, ω_m [rad/s] is the rated angular mechanical speed.

- 2) Calculation of the input power:

$$P_{in} = P_{out}/\eta_d \quad (3)$$

- 3) Calculation of the terminal current:

$$I_t = \frac{P_{in}}{\sqrt{3}V_t \cos(\phi)} \quad (4)$$

the winding connection is star type; Therefore, the phase current (I_{ph}) is equal to the terminal current (I_t). The number of parallel branches (N_p) is also one, and the coil current is equal to the phase current. The coil current is used to calculate the wire size, considering a proper value for J_{sw} . The wire diameter is equal to:

$$d_w = \sqrt{\frac{4 \times I_c}{\pi \times N_{strands} \times J_{sw}}} \quad (5)$$

- 4) The output equation is as follows:

$$P_{out} = G \times D^2 L \times rps \quad (6)$$

here, G is the output coefficient [23],

$$G = \frac{1.11 \times \pi^2 \times k_w \times B_{av} \times ac \times \eta_d \times \cos(\phi)}{\gamma_{emf}} \quad (7)$$

D is the mean diameter,

$$D = (ISD + OSD)/2 \quad (8)$$

L is the stack length,

$$L = (OSD - ISD)/2 \quad (9)$$

, and rps is the rated revolutions per second. γ_{emf} in (7) is the back-EMF ratio,

$$\gamma_{emf} = E_{ph}/V_{ph} \quad (10)$$

in motor mode, the back-EMF ratio is lower than one.

- 5) Calculation of the outer stator diameter:

$$OSD = \sqrt[3]{\frac{8 \times P_{out}}{G \times rps \times (1 + sr)^2 \times (1 - sr)}} \quad (11)$$

here, sr is the split ratio,

$$sr = ISD/OSD \quad (12)$$

The split ratio is a number lower than one, and it should be assumed by designer. Knowing the split ratio, we can calculate ISD . IRD is slightly lower than ISD , and ORD is slightly higher than OSD .

- 6) Calculation of the total air gap flux:

$$\varphi_{total} = B_{av} \times \pi DL \quad (13)$$

knowing the total air gap flux, we can calculate the stator tooth flux,

$$\varphi_{st} = \varphi_{total}/N_s \quad (14)$$

, and the pole flux,

$$\varphi_p = \varphi_{total}/p \quad (15)$$

- 7) Calculation of the desired cross-section area of the stator tooth (d_{Ast} is shown in Fig. 19a):

$$d_{Ast} = \varphi_{st}/B_{st,max} \quad (16)$$

here, $B_{st,max}$ is the maximum permissible flux density level in the stator tooth that is assumed by designer.

- 8) Knowing d_{Ast} , we can calculate w_{ss} from the following equation:

$$d_{Ast} = \frac{\pi DL - N_s w_{ss} L}{N_s} \quad (17)$$

- 9) Calculation of the number of effective turns per-phase:

$$N_{tph} = \frac{E_{ph}}{4.44 \times f_s \times k_w \times \varphi_p} \quad (18)$$

here, f_s is the supply frequency. Knowing N_{tph} , we can calculate N_{tc} using the following equation,

$$N_{tph} = N_{tc} \times \frac{N_s}{3N_p} \quad (19)$$

- 10) Knowing N_{tc} , we can calculate the net copper area of a coil arm (c_{Aca}):

$$c_{Aca} = N_{tc} \times N_{strands} \times d_w \quad (20)$$

- 11) Knowing c_{Aca} , and assuming a suitable number for K_{fill} , we can calculate the gross area of coil arm (g_{Aca}):

$$g_{Aca} = c_{Aca}/K_{fill} \quad (21)$$

g_{Aca} is the total area occupied with the coil arm; it includes copper, insulation, and air.

- 12) Knowing g_{Aca} , we can calculate the coil depth (d_c), and finally depth of the stator slot (d_{ss}),

$$d_c = g_{Aca}/w_c \quad (22)$$

- 13) Fig. 19b shows cross-section surfaces of the stator back iron. Approximately, half of the tooth flux pass through one cross-section. Therefore, d_{sy} is calculated using the following equation:

$$\frac{\varphi_{st}}{2} = B_{sy,max} \times d_{sy} \times L \quad (23)$$

here, $B_{sy,max}$ is the maximum permissible flux density level in the stator yoke that is assumed by designer.

- 14) d_{ty} is calculated using the following equation:

$$\frac{\varphi_p}{2} = B_{ry,max} \times d_{ty} \times L \quad (24)$$

here, $B_{ry,max}$ is the maximum permissible flux density level in the rotor yoke that is assumed by designer.

* **Note:** The magnet depth is determined through magnetic loading and static torque analyses.

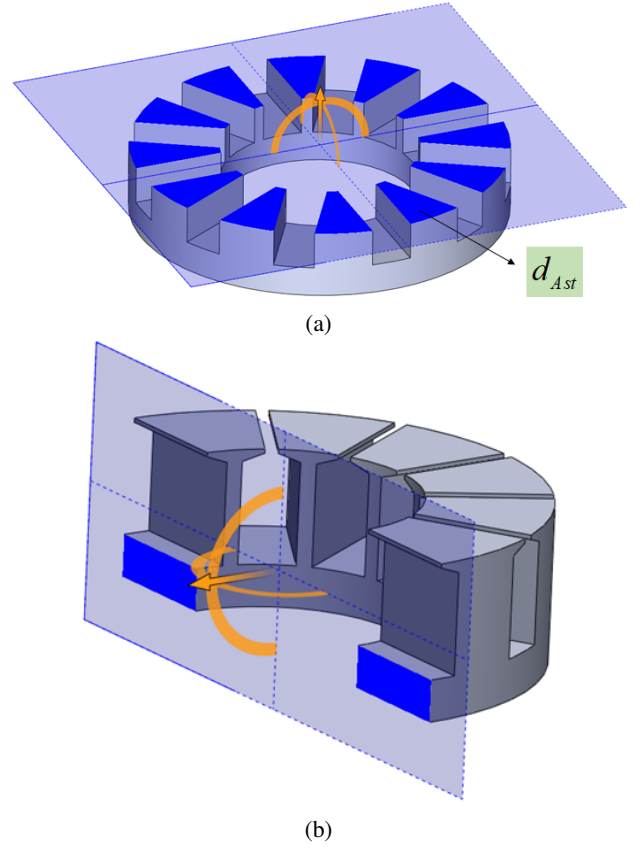


Fig. 19: Cross-sections of the stator core: (a) desired area of the stator tooth, (b) the stator back iron

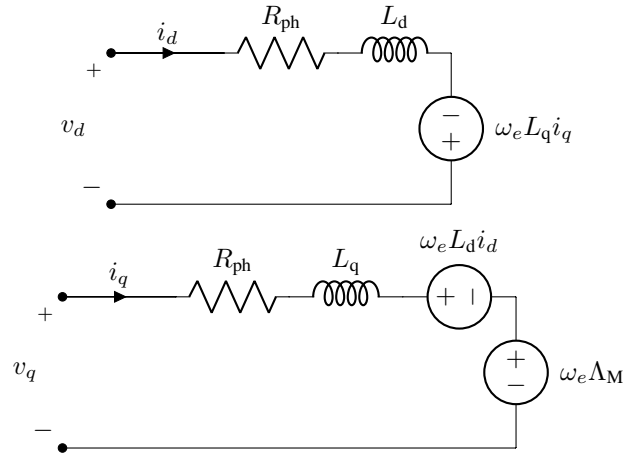


Fig. 20: Dynamic equivalent circuits of the motor in the rotor reference frame (ω_e is the electrical angular speed)

APPENDIX C EQUIVALENT CIRCUITS

Fig. 20 shows the dynamic equivalent circuits of the motor [24]. For a quick calculation of the performance curves, we can solve the equivalent circuit model for different speeds, considering voltage and current limitations.

REFERENCES

- [1] V. Simón-Sempere, A. Simón-Gómez, M. Burgos-Payán, and J. R. Cerquides-Bueno, "Optimisation of magnet shape for cogging torque reduction in axial-flux permanent-magnet motors," *IEEE Transactions on Energy Conversion*, vol. 36, no. 4, pp. 2825–2838, 2021.
- [2] W. Le, M. Lin, K. Lin, L. Jia, and A. Yang, "Design and analysis of a rotor air-cooling enhanced method for axial flux permanent magnet machine with housing-cooling," *IEEE Transactions on Energy Conversion*, vol. 38, no. 3, pp. 2136–2145, 2023.
- [3] M. Gulec and M. Aydin, "Implementation of different 2d finite element modelling approaches in axial flux permanent magnet disc machines," *IET Electric Power Applications*, vol. 12, no. 2, pp. 195–202, 2018.
- [4] D. K. Lim, Y. S. Cho, J. S. Ro, S. Y. Jung, and H. K. Jung, "Optimal design of an axial flux permanent magnet synchronous motor for the electric bicycle," *IEEE Transactions on Magnetics*, vol. 52, no. 3, pp. 1–4, 2016.
- [5] G. Yang, J. Li, and M. Lin, "Design and analysis of novel modular stator axial-flux permanent magnet vernier machine with improved power factor," *IEEE Access*, vol. 11, pp. 108 580–108 590, 2023.
- [6] R. Burke, A. Giedymin, Z. Wu, H. Chuan, N. Bourne, and J. G. Hawley, "A lumped parameter thermal model for single-sided afpm machines with experimental validation," *IEEE Transactions on Transportation Electrification*, vol. 6, no. 3, pp. 1065–1083, 2020.
- [7] P. Vrtic, P. Pisek, M. Hadziselimovic, T. Marcic, and B. Stumberger, "Torque analysis of an axial flux permanent magnet synchronous machine by using analytical magnetic field calculation," *IEEE Transactions on Magnetics*, vol. 45, no. 3, pp. 1036–1039, 2009.
- [8] A. C. Malloy, R. F. Martinez-Botas, and M. Lampérth, "Measurement of magnet losses in a surface mounted permanent magnet synchronous machine," *IEEE Transactions on Energy Conversion*, vol. 30, no. 1, pp. 323–330, 2015.
- [9] S. Javadi and M. Mirsalim, "A coreless axial-flux permanent-magnet generator for automotive applications," *IEEE Transactions on Magnetics*, vol. 44, no. 12, pp. 4591–4598, 2008.
- [10] S. Kahourzade, N. Ertugrul, and W. L. Soong, "Loss analysis and efficiency improvement of an axial-flux pm amorphous magnetic material machine," *IEEE Transactions on Industrial Electronics*, vol. 65, no. 7, pp. 5376–5383, 2018.
- [11] A. Dwivedi, S. k. Singh, and R. K. Srivastava, "Analysis and performance evaluation of axial flux permanent magnet motors," *IEEE Transactions on Industry Applications*, vol. 54, no. 2, pp. 1765–1772, 2018.
- [12] F. G. Capponi, G. D. Donato, and F. Caricchi, "Recent advances in axial-flux permanent-magnet machine technology," *IEEE Transactions on Industry Applications*, vol. 48, no. 6, pp. 2190–2205, 2012.
- [13] P. Vrtić, M. Vražić, and G. Papa, "Design of an axial flux permanent magnet synchronous machine using analytical method and evolutionary optimization," *IEEE Transactions on Energy Conversion*, vol. 31, no. 1, pp. 150–158, 2016.
- [14] B. Guo, Y. Huang, F. Peng, Y. Guo, and J. Zhu, "Analytical modeling of manufacturing imperfections in double-rotor axial flux pm machines: Effects on back emf," *IEEE Transactions on Magnetics*, vol. 53, no. 6, pp. 1–5, 2017.
- [15] Y. Kano, T. Kosaka, and N. Matsui, "A simple nonlinear magnetic analysis for axial-flux permanent-magnet machines," *IEEE Transactions on Industrial Electronics*, vol. 57, no. 6, pp. 2124–2133, 2010.
- [16] X. Yang, D. Patterson, and J. Hudgins, "Design optimization of single-sided axial flux permanent magnet machines by differential evolution," in *2014 International Conference on Electrical Machines (ICEM)*, Conference Proceedings, pp. 1090–1095.
- [17] S. Mohammadi, M. Mirsalim, S. Vaez-Zadeh, and H. Lesani, "Sensitivity analysis and prototyping of a surface-mounted permanent-magnet axial-flux coupler," in *The 5th Annual International Power Electronics, Drive Systems and Technologies Conference (PEDSTC 2014)*, Conference Proceedings, pp. 568–573.
- [18] L. Alberti, E. Fornasiero, N. Bianchi, and S. Bolognani, "Rotor losses measurements in an axial flux permanent magnet machine," *IEEE Transactions on Energy Conversion*, vol. 26, no. 2, pp. 639–645, 2011.
- [19] M. Mirzaei, M. Mirsalim, and S. E. Abdollahi, "Analytical modeling of axial air gap solid rotor induction machines using a quasi-three-dimensional method," *IEEE Transactions on Magnetics*, vol. 43, no. 7, pp. 3237–3242, 2007.
- [20] X. Yang, D. Patterson, J. Hudgins, and J. Colton, "Fea estimation and experimental validation of solid rotor and magnet eddy current loss in single-sided axial flux permanent magnet machines," in *2013 IEEE Energy Conversion Congress and Exposition*, Conference Proceedings, pp. 3202–3209.
- [21] R. Yazdanpanah and M. Mirsalim, "Axial-flux wound-excitation eddy-current brakes: Analytical study and parametric modeling," *IEEE Transactions on Magnetics*, vol. 50, no. 6, pp. 1–10, 2014.
- [22] W. Li, P. Song, S. Mukundan, B. D. S. G. Vidanalage, G. Spehar, V. Russalian, S. Reaburn, and N. C. Kar, "Structural analysis of single-sided axial-flux permanent magnet machines with different magnetic materials," *IEEE Transactions on Magnetics*, vol. 57, no. 2, pp. 1–5, 2021.
- [23] J. Pyrhonen, T. Jokinen, and V. Hrabovcova, *Design of rotating electrical machines*. John Wiley & Sons, 2013.
- [24] R. Krishnan, *Permanent magnet synchronous and brushless DC motor drives*. CRC press, 2017.